Determination of Interstellar He Parameters using 5 years of data from the Interstellar Boundary Explorer – beyond closed form approximations

N. A. Schwadron[1], E. Möbius, and T. Leonard

University of New Hampshire, Durham, NH, 03824

S. A. Fuselier and D. J. McComas[2]

Southwest Research Institute, San Antonio, TX 78228, USA

D. Heirtzler, H. Kucharek, and F. Rahmanifard

University of New Hampshire, Durham, NH, 03824

M. Bzowski, M. A. Kubiak, J. M. Sokół, and P. Swaczyna

Polish Academy of Sciences Space Research Centre, Warsaw, Poland

P. Frisch

U. Chicago, Chicago, IL, 60637

ABSTRACT

Interstellar He represents a key sample of interstellar matter that, due to its high first ionization potential, survives the journey from beyond our solar system's heliospheric boundaries to Earth. Ongoing analysis of interstellar neutral (ISN) He atoms by the Interstellar Boundary Explorer (IBEX) has resulted in a growing sophistication in our understanding of local interstellar flow. A key feature of the IBEX observations near perihelion of the ISN trajectories is a narrow "tube" of approximately degenerate interstellar parameters. These degenerate solutions provide a tightly coupled relationship between interstellar flow longitude and latitude, speed, and temperature. However, IBEX analysis resulting in a specific solution for inflow longitude, inflow speed, temperature and inflow latitude was accompanied with a sizeable uncertainty along the parameter tube. Here, we use the three-step method to find the interstellar parameters: 1) the

[1]also, Southwest Research Institute, San Antonio, TX 78228, USA

[2]also, University of Texas at San Antonio, San Antonio, TX 78228, USA

ISN He peak rate in ecliptic longitude determines uniquely a relation (as part of the tube in parameter space) between the longitude $\lambda_{ISN\infty}$ and the speed $V_{ISN\infty}$ of the He ISN flow at infinity; 2) the ISN He peak latitude (on the great circle swept out in each spin) is compared to simulations to derive unique values for $\lambda_{ISN\infty}$ and $V_{ISN\infty}$ along the parameter tube; 3) the angular width of the He flow distributions as a function of latitude is used to derive the interstellar He temperature. For simulated peak latitudes, we use a relatively new analytical tool that traces He atoms from beyond the termination shock into the position of IBEX and incorporates the detailed response function of IBEX-Lo. By varying interstellar parameters along the IBEX parameter tube, we find the specific parameters that minimize the chi-square difference between observations and simulations. The new computational tool for simulating neutral atoms through the integrated IBEX-Lo response function makes no assumptions or expansions with respect to spin axis pointing or frame of reference. Thus, we are capable of moving beyond closed form approximations and utilize observations of interstellar He during the complete 5 year period from 2009 to 2013 when the primary component of interstellar He is most prominent. Chi-square minimization of simulations compared to observations results in a He ISN flow longitude $75.6° \pm 1.4°$, latitude $-5.12° \pm 0.27°$, speed 25.4 ± 1.1 km/s, and temperature 8000 ± 1300 K, where the uncertainties are related and apply along the IBEX parameter tube. This paper also provides documentation for a new release of ISN data and associated model runs.

Subject headings: Local Interstellar Medium, Heliosphere

1. Introduction

Interstellar neutral (ISN) flow measurements made by the Interstellar Boundary Explorer mission (McComas et al. 2009) include the first direct H, He, O (Möbius et al. 2009), and D (Rodríguez Moreno et al. 2013, 2014) flow observations and a determination of the LIC Ne/O ratio (Bochsler et al. 2012; Park et al. 2014). Each of the interstellar neutral species (e.g., H, D, He, O, Ne, etc.) has a primary component associated with atoms that flow directly through the heliosphere and likely a secondary component associated with atoms that have interacted in the heliosheath. Primary components are only modified due to loss through ionization (charge-exchange with the solar wind, photo-ionization, electron impact ionization) and gravitational effects. Therefore, each neutral species' primary component provides a relatively pristine reflection of its local interstellar velocity distribution, which through analysis yields the best available estimate of the local interstellar bulk flow velocity and the temperature of the species.

The secondary components of neutral atoms are created by charge-exchange interactions (collisions and electron exchange between interstellar neutral matter and charged plasma particles) between the primary ISN component and the plasma in the heliosheath. These modifications of the secondary components reflect, in part, the heated, deflected and slowed plasma in the outer heliosheath. Recent IBEX measurements have revealed what is likely the secondary component of He, dubbed the Warm Breeze (Kubiak et al. 2014). The secondary component is also observed by IBEX in the ISN O signal (Möbius et al. 2009; Park et al. 2015).

In addition to the photo-ionization loss and complex charge-exchange effects that modify the ISN components (Bzowski et al. 2013a), interstellar H atoms also experience a large force associated with radiation pressure roughly comparable in magnitude but opposite in direction to the force of gravity (Bzowski et al. 2013b). This radiation pressure is exerted due to atoms' resonant absorption and re-emission of solar Ly-α. Deflection of the primary ISN H flow by solar radiation pressure was revealed by IBEX from in situ observations for the first time (Schwadron et al. 2013; Katushkina et al. 2015).

The measurements of ISN He are uniquely important for characterizing the properties of the local interstellar medium (LISM). Due to the high first ionization potential of He, these atoms are relatively unaffected by charge-exchange compared to other ISN species with lower first ionization potentials. Combined with its high universal abundance (second only to H), ISN He has a large primary component with a distribution function that can be used to yield the most accurate determination of the LISM neutral temperature and bulk velocity. IBEX observations of interstellar neutral He atoms have a signal to background ratio of > 1000. This remarkable sensitivity enables in-depth study of the He flow characteristics (Bzowski et al. 2012; Möbius et al. 2012; McComas et al. 2012a, 2015), and promises to become the most detailed and accurate direct measurement of the ISN flow vector and temperature to date. In addition, these measurements will likely illuminate the possible departures from the perfect Maxwell-Boltzmann distribution (Kubiak et al. 2014; Sokół et al. 2015a).

IBEX observations also pose significant new challenges (Möbius et al. 2015b; McComas et al. 2015; Leonard et al. 2015). Due to the observation of the ISN flow with IBEX over a limited range of longitudes within the ecliptic plane, the resulting ISN flow vector and temperature are constrained to a tube in the four-dimensional parameter space consisting of inflow longitude $\lambda_{ISN\infty}$, latitude $\beta_{ISN\infty}$, speed $V_{ISN\infty}$, and temperature $T_{ISN\infty}$. These parameters are tightly coupled through celestial mechanics, yet with a degeneracy that provides for a sizeable allowable range

(Bzowski et al. 2012; Möbius et al. 2012; McComas et al. 2012a). While the allowable range of parameters included the previously established ISN flow vector by Ulysses measurements (Witte et al. 2004; Witte 2004; Möbius et al. 2004), the interstellar temperature from IBEX measurements for the same ISN flow vector was much higher than obtained previously (Möbius et al. 2012, 2015b; Bzowski et al. 2012). The results for the optimum fit to IBEX measurements suggested a flow vector different by 3° in longitude from and a lower inflow speed (Bzowski et al. 2012; Möbius et al. 2012) than determined by Ulysses (Witte et al. 2004), but with a temperature that matched the Ulysses results (Witte 2004).

Potential ramifications of these results, such as the absence of a strong heliospheric bow shock (McComas et al. 2012a) and the possibility of temporal variations in the ISN flow direction over the past 40 years of the space age (Frisch et al. 2013, 2015) were explored. This work lead to important debates on the nature of the bow shock (Zieger et al. 2013; Scherer & Fichtner 2014; Zank et al. 2013) as well as a dialog about the potential for or lack thereof temporal variations (Lallement & Bertaux 2014; Frisch et al. 2015) in the ISN flow. The body of work motivated a reassessment of the Ulysses GAS observations (Katushkina et al. 2014; Bzowski et al. 2014; Wood et al. 2015), which suggested significantly increased temperature and widened error bars compared to the original Ulysses results (Witte 2004). In addition, it was found that small differences in the ISN flow vector ($\lambda_{ISN\infty}$, $\beta_{ISN\infty}$, $V_{ISN\infty}$) have profound effects on the orientation of the $\mathbf{B}_{ISM} - \mathbf{V}_{ISM}$ plane, which influences the large-scale structure of and the plasma flow around the heliosphere (Bzowski et al. 2012; Möbius et al. 2015b).

This study is part of a coordinated set of papers on interstellar neutrals as measured by IBEX; McComas et al. (2015) provides an overview of this Special Issue. The purpose of our study is twofold. We extend the analytic framework initially developed by Lee et al. (2012) for solving neutral atoms trajectories. Instead of adopting approximations to yield closed form solutions in the Earth frame of reference (see also, Lee et al. 2015), we integrate over the complete IBEX-Lo response function (Schwadron et al. 2009) in the frame of reference of the spacecraft to simulate neutral atom rates. We then utilize a larger amount of IBEX data (5 years from 2009 through 2013) together with the improved model of interstellar He atoms to reduce uncertainties in the determination of the ISN flow vector and temperature.

The paper is organized as follows. Section 2 discusses the observations utilized for the study. Section 3 details the model utilized to simulate observed neutral atom rates by integrating an analytic model of neutral trajectories over the instrument response. Section 4 discusses the analysis of observations. In this section, we first repeat the analysis of Leonard et al. (2015) and then discuss a broader application over five years of IBEX data. Section 5 outlines the data release and Section 6 concludes the paper by outlining implications for our understanding of the properties of the LISM.

2. Observations

IBEX has two energetic neutral atom (ENA) sensors for remotely mapping the global heliosphere and making direct measurements of interstellar neutral atoms (McComas et al. 2009). The IBEX-Lo sensor measures neutral atoms from 10 eV to 2 keV and includes a time-of-flight analysis to provide compositional information (Fuselier et al. 2009; Möbius et al. 2009). The IBEX-Hi sensor measures ENAs from $\sim$300 eV to 6 keV (Funsten et al. 2009).

The IBEX-Lo entrance system accepts incoming neutral atoms through a large-area collimator with a 7° full width at half Maximum (FWHM). After passing through the collimator, neutrals collide with a conversion surface where a small fraction of these incoming atoms are converted into negative ions. The negative ions are then filtered based on their energy and charge by an electrostatic analyzer. After post acceleration to boost their energy, negative ions pass through a time-of-flight system, which, together with the energy and charge measurements, determines the mass and therefore the atomic species of these particles.

The conversion surface acts differently for differing atomic species. Incoming He atoms predominantly sputter H^- ions. During optimal ISN He observing periods near the beginning of each year, the motion of IBEX, which moves with Earth around the Sun at $\sim$30 km s^{-1}, opposes the velocity of incident neutral atoms. ISN He atoms, based on IBEX-Lo observations, move at an average speed of $\sim$22-27 km s^{-1} relative to the Sun in the outer heliosphere. The He atoms that make it in to 1 AU increase their kinetic energy and speed to $\sim$50 km s^{-1} due to the Suns gravitational attraction. During the IBEX-Lo He observing periods, in the frame of the spacecraft, incident ISN He atoms have typical speeds of $\sim$80 km s^{-1} into the IBEX-Lo sensor. This implies a kinetic energy of $\sim$130 eV.

The general methodology of IBEX ISN He observations are detailed by Möbius et al. (2012), and summarized here. The incident energy during He observing periods near the beginning of the year is similar to the 110 eV energy of step 4 of the IBEX-Lo electrostatic analyzer (ESA). While the ISN He temperature slightly broadens the angular distribution at 1 AU, the incoming ISN He distribution is remarkably narrow and beam-like. The IBEX-Lo ESA steps admit a broad range of energies ($\Delta E/E \sim 0.7$), so the vast majority of these He atoms fall within ESA step 4. Sputtered products of the incident He atoms have energies less than the parent atom. Therefore, the sputtered H^- ions are observed in ESA step 1 through ESA step 4. The peak count rates of sputtered products generated by incident He with kinetic energy

$\sim$ 130 eV occurs in ESA step 3 and ESA step 2. Therefore, in the IBEX orbits where the IBEX-Lo sensor is oriented to allow large fluxes of ISN He atoms into the collimator, we observe the largest count rate in ESA step 3 and step 2, comparable count rates in ESA step 1, and sizeable, but substantially lower rates in ESA step 4. These energy signatures provide a straightforward identification of ISN He in IBEX observations (Möbius et al. 2012).

IBEX is a Sun-pointed spinner with the sensor field-of-view pointing at 90° from the spin axis. The IBEX-Lo sensor sweeps out a great circle on the celestial sphere roughly every 15 s. During the season of prime interstellar He viewing in the spring of each year the Earth and thus IBEX ram into the oncoming ISN flow, which covers a limited spin phase range close to the ecliptic. The ISN He flow rate peaks around February 8 each year. As shown by Lee et al. (2012) and Möbius et al. (2012) the ecliptic longitude of the ISN flow peak determines uniquely a relation (as part of the tube in parameter space) between the longitude $\lambda_{ISN\infty}$ and the speed $V_{ISN\infty}$ of the He ISN flow at infinity based on the hyperbolic trajectory equation for interstellar atoms. This is the first step of a three-step ISN flow analysis followed here, which is described in detail in Möbius et al. (2015a) and worked out analytically in Lee et al. (2012) and Lee et al. (2015). The second step takes advantage of the fact that the peak latitude (on the great circle swept out in each spin) of the He ISN flow changes with the longitude of the spacecraft and represents a fundamental measurement that can be compared to simulations to derive unique values for $\lambda_{ISN\infty}$ and $V_{ISN\infty}$ along the functional dependence of the parameter tube. In a third step, the angular width of the flow distributions as a function of latitude is used to derive the temperature of interstellar He.

3. Integrated Instrument Response Model using Analytic Trajectories

The simulated distributions analyzed here are an extension of the analytic trajectory calculations from Lee et al. (2012). We start from the hot model (Thomas 1978; Fahr 1979; Wu & Judge 1979) of ISN gas in the heliosphere and integrate the signal through the detailed response function of IBEX-Lo. Individual trajectories of neutral atoms are traced from beyond the heliosphere in to 1 AU, where they can be observed by IBEX. The survival probability of these neutral atoms is taken into account. This probability assumes that the ionization rate is constant at a given location and falls off with the inverse square of heliocentric radius, which is appropriate for photo-ionization, and charge exchange losses on average. Sokół et al. (2015b) describe many of the details that are similar to our model's implementation, including the formulation of Kepler hyperbolic trajectories, and the challenges that this type of modeling must address.

At the location of the IBEX-Lo instrument, the model performs a series of numerical integrations to account for the instrument response (Schwadron et al. 2009; Möbius et al. 2009; Schwadron et al. 2013). These integrations are performed for the observation geometry specific to a given moment in time and include integration over 6° spin-sectors (there are 60 total spin sectors covering each 360° rotation), integration over the viewing angles of the collimator, and integration over energy (see Schwadron et al. 2013). The integration over the collimator takes into account the detailed point-spread function of IBEX-Lo (Schwadron et al. 2009). We summarize the integrations as follows. For each spin phase within a given spin-sector, and each viewing position along the collimator, there is a single incident vector for an atom passing into the sensor. For a given incident atom energy, the atoms incident vector can be associated with the atoms velocity $\mathbf{V}$ in the inertial frame. With knowledge of the atoms velocity and the position ($\mathbf{R}$) of the spacecraft, the neutral atoms trajectory can be traced back through the heliosphere and into the interstellar medium to determine the velocity of the atom at infinity $\mathbf{V}_\infty$. The formulae for these transformations can be found in Lee et al. (2012) and Sokół et al. (2015b). The distribution function at the spacecraft is equated with the distribution function outside the heliosphere multiplied by the survival probability.

The distribution function at the spacecraft is used to find the differential energy flux. It is then integrated over energy (from 30 eV to 230 eV) to find the net flux of atoms into the instrument in the specified look direction in longitude and spin phase. Notably, this integration to form the total flux must be done very carefully since the distribution is sharply peaked. In the numerical energy integration, we first find the peak of the energy distribution and then integrate using an adaptive energy grid. We have tested the energy integration, which was found to be accurate to high-order (at least sixth-order in the step-size of the energy grid). We have also shown convergence of the integrated fluxes to $< 0.05\%$.

The rate-per-steradian of measured atoms for the specific look direction is proportional to the flux of atoms into the instrument. Look directions are integrated over collimator (the collimator response function has been released in IBEX data release #6, http://ibex.swri.edu/ibexpublicdata/Data_Release_6/) and averaged over spin phase within the 6° sector to simulate the rate of atoms measured by IBEX-Lo. This methodology allows us to make direct comparisons between results of the model and the count rates observed for a specific orientation of the instrument and position of the spacecraft.

4. Observational Analysis

The distribution of rates in spin-sectors generally peaks for spin-sectors close to the ecliptic plane. In fact, this peak in the spin-sector distribution can be solved for quite accurately by fitting the spin-sector rate distribution. The derived peak spin-phase (or equivalently, the peak latitude) is a function of the spacecraft longitude that depends sensitively on the longitude and latitude at infinity of the inflowing neutral atoms (see also, Möbius et al. 2012). In other words, the distribution of peak latitudes is a function of observer longitude that depends sensitively on interstellar parameters. By comparing the distributions of peak latitudes vs. observer longitude between simulations and observations, we can in principle recover the interstellar parameters. The advantage of this technique is that it is insensitive to relatively smooth backgrounds.

We are left with the exercise of searching for the best agreement between simulations and observations for a particular set of interstellar parameters. Evaluation of the "best" parameters is done using a χ^2 minimization where the χ^2 is expressed

$$\chi^2 = \sum_{i=1}^{N} \frac{(\beta_{oi} - \beta_{si})^2}{\sigma_{oi}^2} \tag{1}$$

indicating a summation over the square difference between the observed (β_{oi}) and simulated (β_{si}) peak latitude divided by the variance (σ_{oi}^2). Here, the simulated peak latitude β_{si} is found precisely using a derivative-based prediction-correction scheme. The reduced $\tilde{\chi}^2 = \chi^2/M$ where M is the number of free parameters, $M = N - n - 1$ and n is the number of variables used in the fit.

Comparison with the analytic models of Lee et al. (2012) and Lee et al. (2015) has shown that these peaks in the spin-phase distribution are accurate to within 0.01° (Möbius et al. 2015a). Notably, the spin-phase peak referred to here lies within a given spin-phase sector; the model is not limited to the particular spin-phase binning utilized by the instrument. The variance σ_{oi}^2 is based on sum of the Poisson variance using counting statistics and the square of 0.05° pointing uncertainty. The 0.05° pointing uncertainty arises from the time tagging of events no finer than one of our 4.1 ms time ticks, or equivalent to $\sim$0.1°. The events are sorted into 6° bins, but because of the granularity of individual events, the boundaries for sorting the events have a small, essential random fluctuation leading to an average uncertainty of $\pm$0.05°. The summation in equation (1) extends over every instance of a peak latitude at a given observer longitude.

The four-dimensional parameter tube that was developed by Möbius et al. (2012) provides an important simplification for the present analysis. We utilize the equations for the parameter tube expressed by McComas et al. (2012a) for the inflow latitude

$\beta_{ISN\infty}$, the speed $V_{ISN\infty}$, and temperature $T_{ISN\infty}$ as a function of observer longitude $\lambda_{ISN\infty}$. Utilizing all five years of data (2009-2013), we have also varied the latitude $\beta_{ISN\infty}$ to check whether the original parameter tube detailed by McComas et al. (2012a) remains a valid. We find the $\tilde{\chi}^2$ minimum associated with parameter variation of the inflow latitude $\beta_{ISN\infty}$ with the interstellar longitude $\lambda_{ISN\infty}$ specified by a characteristic line orthogonal to the parameter tube:

$$\lambda_{ISN\infty} = \lambda_0 - \left.\frac{\partial\beta_{ISN\infty}}{\partial\lambda_{ISN\infty}}\right|_{\lambda_0,\beta_0} (\beta_{ISN\infty} - \beta_0) \tag{2}$$

where $\partial\beta_{ISN\infty}/\partial\lambda_{ISN\infty}$ is the gradient of the of the $\beta_{ISN\infty}$ along the 4-D parameter tube. Here λ_0 and β_0 are the longitude and latitude at a specific crossing point on the parameter tube. The other two parameters $T_{ISN\infty}$ and $V_{ISN\infty}$ are varied in this case along the parameter tube.

Figure 1 shows an example of this $\tilde{\chi}^2$ minimization for $\beta_{ISN\infty}$ in the 2013 ISN season, which tests whether relations of the parameter tube remain accurate. The intersection with the parameter tube is at position: $\beta_0 = -5.12°$, $T_0 = 7983$ K, $\lambda_0 = 75.6°$ and $V_0 = 25.4$ km/s. Individual values of the $\tilde{\chi}^2$ (circles in Figure 1) are fit to a quadratic curve given by $\tilde{\chi}^2(\beta_{ISN\infty}) = A_0 + A_2(\beta_{ISN\infty} - \beta_0)^2$ where $A_0 = 1.37$, $A_2 = 11.59$ and $\beta_0 = -5.12°$. The $\tilde{\chi}^2$ fit uncertainty (see Appendix B of Schwadron et al. 2013) is given by $\delta\beta = \sqrt{A_0/(MA_2)}$ where M is the number of free parameters in the fit. The number of data points used for each $\tilde{\chi}^2$ value is $N = 45$ and there is $n = 1$ variable ($\beta_{ISN\infty}$) used in the fit, so that $M = N - n - 1 = 43$. Therefore, the result of the $\tilde{\chi}^2$ minimization as a function of $\beta_{ISN\infty}$ for 2013 data is an inflow latitude of $\beta_{ISN\infty} = -5.12° \pm 0.05°$ where the uncertainty includes only that derived from the $\tilde{\chi}^2$ fit. This $\tilde{\chi}^2$-minimum inflow latitude is practically identical to the inflow latitude specified by the relations associated with the parameter tube, $\beta_{ISN\infty} = -5.12° \pm 0.22°$. The larger uncertainty in the parameter tube width is the result of additional uncertainties such as the uncertainty in pointing knowledge that were included in the parameter tube specification.

The result shows consistency in the parameter tube position derived using the more recent IBEX data. This same exercise can be repeated by varying the inflow latitude with other parameters varied orthogonal to the parameter tube starting at different tube intersections or using different ISN seasons. The result is the same as the example shown in Figure 1: the parameter tube derived by Möbius et al. (2012) and stated by McComas et al. (2012a) remains a good representation of the approximately degenerate solutions of ISN parameters from IBEX observations.

The simulations are used to model peak latitudes in the frame of the spacecraft for each orientation of the spin-axis during a given observation. The mission ephemeris

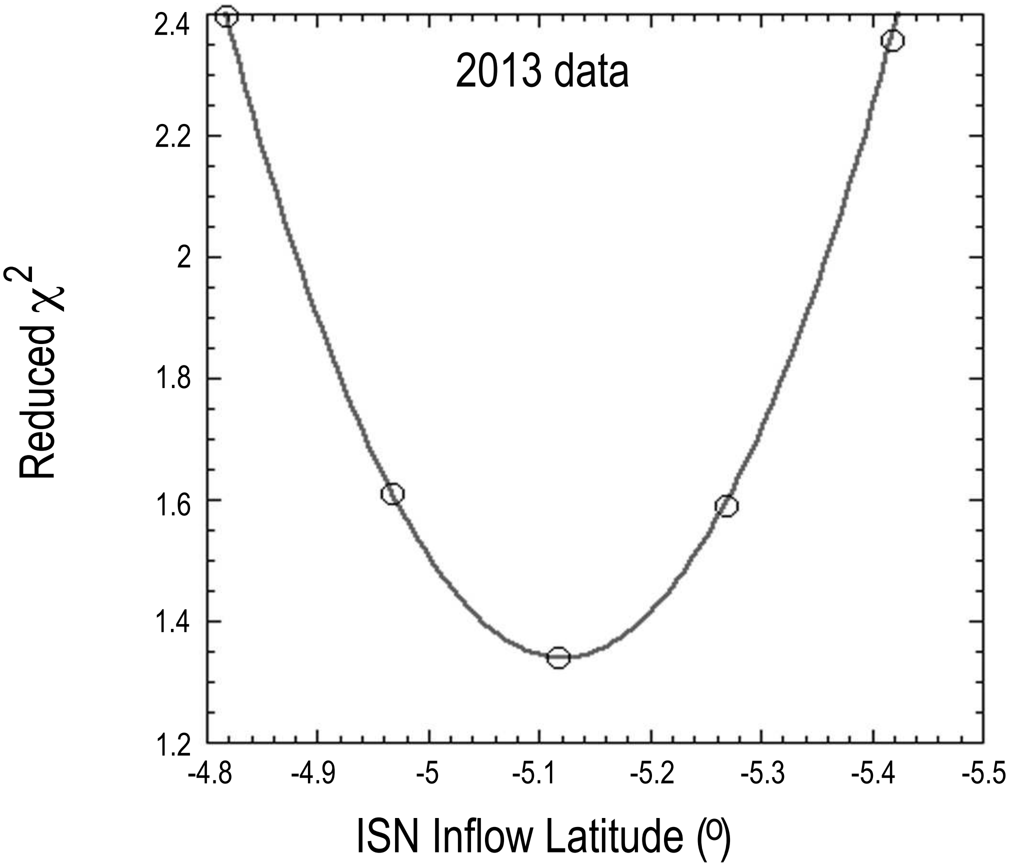

Fig. 1.— Reduced $\tilde{\chi}^2$ dependence for the simulated versus observed peak distributions for the data set from the 2013 ISN season. We vary the ISN flow latitude and other ISN parameters along a path that is orthogonal to the 4-D ISN parameter tube (McComas et al. 2012a) in order to check whether the original specifications of the parameter tube remain valid. The intersection of the parameter path with the 4-D tube is: $\beta_{ISN\infty} = -5.12^\circ$, $T_{ISN\infty} = 7983$ K, $\lambda_{ISN\infty} = 75.6^\circ$ and $V_{ISN\infty} = 25.4$ km/s. Individual values of the $\tilde{\chi}^2$ are fit to a quadratic given by $\tilde{\chi}^2(\beta_{ISN\infty}) = A_0 + A_2(\beta_{ISN\infty} - \beta_0)^2$ where $A_0 = 1.37$, $A_2 = 11.59$ and $\beta_0 = -5.12^\circ$. The result of the $\tilde{\chi}^2$ minimization reveals $\beta_{ISN\infty} = -5.12^\circ \pm 0.05^\circ$ where the uncertainty includes only that derived from the $\tilde{\chi}^2$ fit. The corresponding inflow latitude specified by the relations associated with the parameter tube is $\beta_{ISN\infty} = -5.12^\circ \pm 0.22^\circ$ where additional uncertainties are included such as uncertainty in pointing knowledge. The result demonstrates robustness in the 4-D parameter tube relation specified by McComas et al. (2012a).

(using SPICE, see http://naif.jpl.nasa.gov/naif/spiceconcept.html) is used to specify the position and velocity of the spacecraft as a function of time. These details are important in that the model is not restricted spin-axis to orientations within the ecliptic or to exact Sun-pointing, and the frame of reference is precisely that of the sensor. (See Sokół et al. (2015b), for the effect of pointing variation on the observed He rate distributions as a function of spin-phase and observer longitude).

We have performed numerous validation exercises, several of which we detail here. The first of these validation exercises studies the effect of interstellar Mach number on the peak latitude. The concept is that a large Mach number in the interstellar flow renders extremely peaked distributions. More specifically, the flow speed for He is much larger than the thermal speed for He so that the distribution function is quite narrow. These peaked distributions behave like a pencil beam, and the peak latitude in the simulated distribution integrated over the collimator and spin-angle should converge with the absolute peak latitude from the center of the collimator at the energy that maximizes the differential flux incident on the instrument (Figure 2). Conversely, as the Mach number of the interstellar distributions decreases, the neutral distribution function broadens and should reveal differences between the peak latitude from the complete integrated instrument response and the absolute peak latitude from the center of the collimator. Generally, the neutral latitude distributions are asymmetric about the peak with a tendency toward increased fluxes at latitudes below the peak as compared to fluxes at latitudes above the peak. This asymmetry is created by the combination spacecraft's large azimuthal motion, ~ 30 km/s in the Earth's ram direction due to Earth's motion about the Sun, and the latitude of the flow that comes from above the ecliptic plane. Therefore, as the distribution of neutrals broadens, the integration over the collimator tends to shift the peak latitude toward the equator ($0°$ latitude). For typical interstellar speeds ($\sim$26 km/s) and interstellar temperatures up to $\sim$8000 K, the derived peak latitude from the distribution is within $\sim 0.05°$ of the absolute peak latitude.

We begin our analysis to derive ISN parameters by applying our model to one of the data sets examined by Leonard et al. (2015). This previous analysis broke up IBEX data into three groups based on the ecliptic latitude ϵ_z of spin-axis pointing: group 1 had $\epsilon_z \sim 0.7°$ in 2009-2010, group 2 had $\epsilon_z \sim 0.0°$ in 2012-2014, and group 3 had $\epsilon_z \sim -4.9°$ in 2014. However, only group 2 with $\epsilon_z \sim 0°$ could strongly constrain the interstellar parameters, because additional expansions in the analytic treatment were applied for cases $\epsilon_z \neq 0°$, which led to a visible, but unphysical dependence of the derived ISN parameters on ϵ_z. As a starting point for the current work, we have analyzed the time periods and observations for group 2 ($\epsilon_z \sim 0°$) during 2012, 2013, and 2014 when the spin-axis was less than 0.2° out of the ecliptic plane. This provides the basis for direct comparison with the previous results of Leonard et al. (2015), which were carried out with a fully analytic treatment. More specifically, we

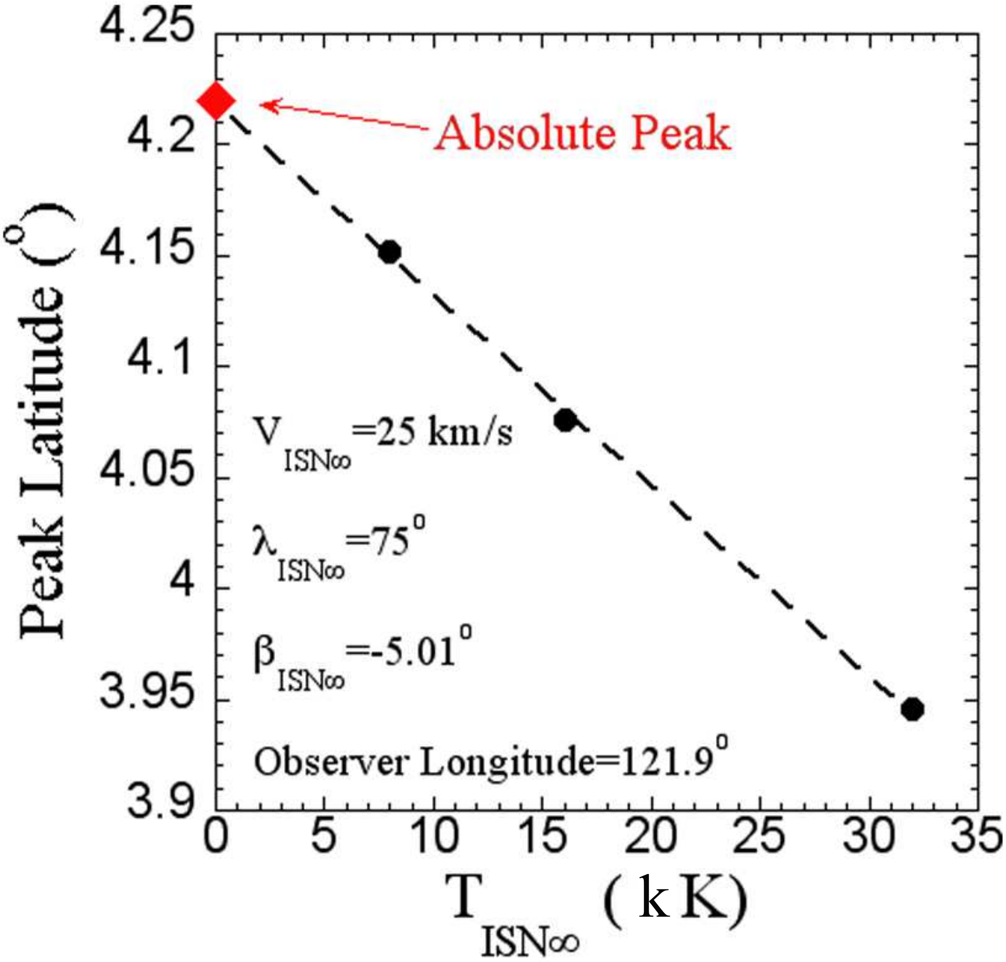

Fig. 2.— Simulated peak latitude as a function of interstellar temperature compared to the absolute peak latitude from the center of the collimator and the energy associated with maximum differential flux. Notably, the simulated peak latitude that includes full integration over the collimator, energy and spin phase converges to the absolute peak in the distribution for small temperature (and therefore large Mach number). This represents a stringent test of the simulation.

analyze: orbit arcs 153b, 154a, 154b, 156a, 157a, and 158a in 2012; orbit arcs 193b, 194a, 195a, 196a, and 197a in 2013; and orbit arcs 234b, 236b, 237b, and 238a in 2014.

The observed IBEX data in each orbit (or orbit arc) analyzed includes the peak spin-phase latitude and its uncertainty during five time periods throughout the orbit (or orbit arc). Each of these five time periods includes accumulation times as large as possible to minimize uncertainties. The main limitation in the accumulation time is the presence of spurious backgrounds (Galli et al. 2014; Fuselier et al. 2014; Galli et al. 2015) including magnetospheric neutrals, suprathermal ions, energetic particles, and solar wind deflected into the instrument. The key challenge in defining good observational periods (called "ISN goodtimes": Möbius et al. 2012; Leonard et al. 2015; Möbius et al. 2015a) is eliminating all possible background sources. During periods when backgrounds are not present, accumulation times can be large, up to 1 day. During periods with intermittent backgrounds, accumulation times can be small, down to 30 min. The average accumulation time is 8 hours. Our model was run given a specific set of interstellar parameters at the average time (or time-center) in each time period analyzed. A specific $\tilde{\chi}^2$ deviation between the simulation and the observations was derived for each set of interstellar parameters, Figure 3. These parameters were then varied along the parameter tube and across it to determine the parameters associated with the $\tilde{\chi}^2$ minimum. In this case, we found $\tilde{\chi}^2$ deviations at 10 different values of $\lambda_{ISN\infty}$ (with the other three ISN parameters varied according to the relations of the 4-D parameter tube) and fit these data to a quadratic, which yields

$$\tilde{\chi}^2(\lambda_{ISN\infty}) = A_0 + A_2(\lambda_{ISN\infty} - \lambda_0)^2 \tag{3}$$

where $A_0 = 1.37$, $A_2 = 0.0076$ and $\lambda_0 = 75.8°$. The $\tilde{\chi}^2$ fit uncertainty is $\delta\lambda = \sqrt{A_0/(MA_2)}$ where the number of data points used in $\tilde{\chi}^2$ is $N = 75$ and, accordingly, the number of free parameters is $M = 73$. Therefore, the $\tilde{\chi}^2$ minimum is $\lambda_{ISN\infty} = 75.8°$ and the fit uncertainty is 1.57°. The result of this analysis is shown in Figure 3 and listed in Table 1.

The actual data points and best-fit simulation results are shown in Figure 4. The figure includes the peak latitude corresponding to the left vertical axis as a function of observer longitude. We also show the spin axis latitude (blue) corresponding to the right vertical axis. Simulation parameters include not only the interstellar parameters, but also the spin-axis pointing, the observer longitude and latitude, and the position of the spacecraft. This renders the simulation results sensitive to detailed characteristics of the spacecraft and sensor orientations. Therefore, for every data point (peak latitude) observed by IBEX, we have a corresponding simulation point. In addition, because observing times depend on finding time periods when backgrounds are minimized, the data points are not necessarily spaced uniformly in

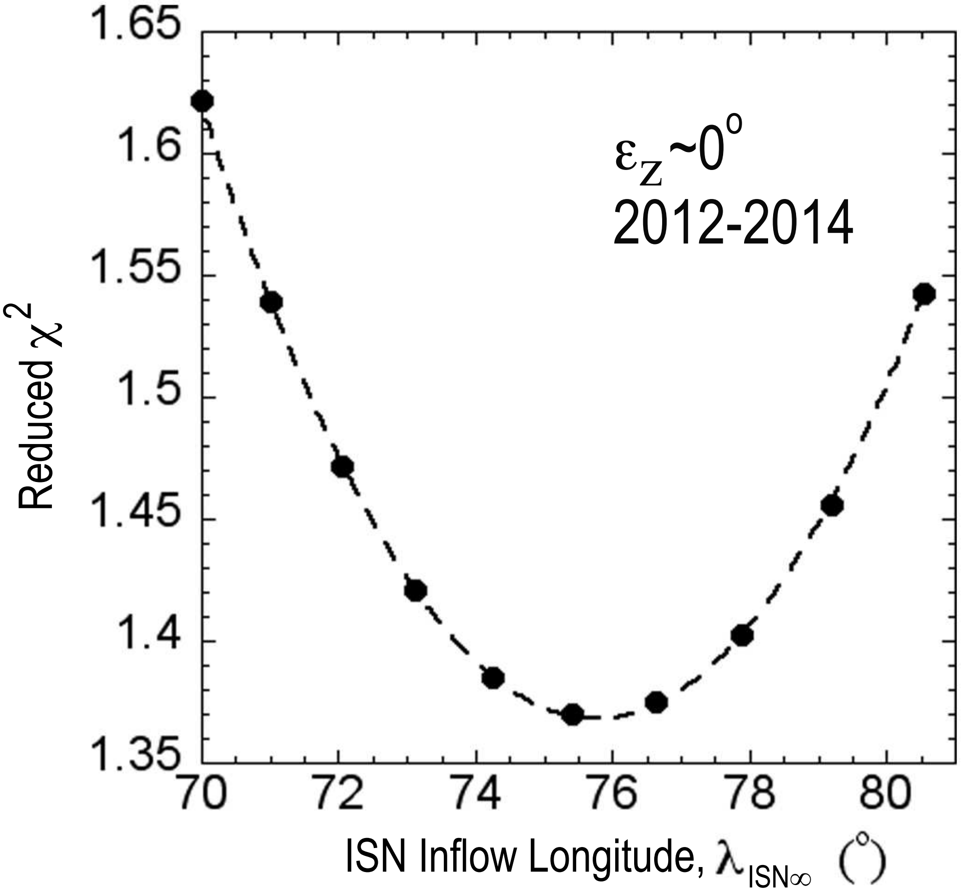

Fig. 3.— Reduced $\tilde{\chi}^2$ dependence for the simulated versus observed peak distributions for the data set studied by Leonard et al. (2015) with the spin axis oriented within 0.2° of the ecliptic. The $\tilde{\chi}^2$ minimum is found for an inflow longitude of $\lambda_{ISN\infty} = 75.8° \pm 1.8°$ which is comparable to the result derived by Leonard et al. (2015) of $\lambda_{ISN\infty} = 74.5° \pm 1.7°$ and Bzowski et al. (2015) of $\lambda_{ISN\infty} = 75.3° \pm 1.7°$ for the same data set. The individual $\tilde{\chi}^2$ values are fit to a quadratic curve, $\tilde{\chi}^2(\lambda_{ISN\infty}) = A_0 + A_2(\lambda_{ISN\infty} - \lambda_0)^2$ where $A_0 = 1.37$, $A_2 = 0.0076$ and $\lambda_0 = 75.8°$.

observer longitude. Another element of variability specific to the $\epsilon_z \sim 0.0°$ case is that there are only specific periods that have the necessary spin-axis pointing.

We next perform the $\tilde{\chi}^2$ minimization using all available data from 2009 through 2013. This procedure yields both a $\tilde{\chi}^2$ minimization for the complete data set (Figure 5 and Table 2) and $\tilde{\chi}^2$ minima for each individual year of observations (Table 3). The uncertainties are formed from the fit, statistical and pointing uncertainties, as detailed in the previous application to the data set used by Leonard et al. (2015).

Figure 6 shows the complete data set in comparison to the optimum simulation. In Figure 6, we have also included a comparison to the 2014 data set. In 2014, note the cluster of observed data points for observer longitudes near 135° and 125°. These are the data that drive the $\tilde{\chi}^2$ fit out of the acceptable range, and each of these data points is associated with a spin-axis pointing of $\epsilon_z \sim 4.9°$. Intervening periods with $\epsilon_z \sim 0°$ appear in much closer agreement with the simulation. The reason for the disagreement for observer longitudes near 135° and 125° remains a puzzle.

There is significant year-to-year variation in the derived LISM parameters (Table 3). The standard deviation of inflow longitude is 1.95°. This issue is detailed by Möbius et al. (2015a) and shown to be at least partially a natural outcome of random Poisson fluctuations in the data. Specifically, Möbius et al. (2015a) include Poisson fluctuations based on counting statistics in simulated rates. They then find latitudinal peaks in the distribution and perform a $\tilde{\chi}^2$ minimization using these simulations over a season (consisting of a range of observer longitudes with a spin-axis pointing in the ecliptic plane). Repeating this trial five times with independent random fluctuations, the $\tilde{\chi}^2$ minimized inflow longitudes converge to within 0.5° of the inflow longitude used in the simulations. The standard deviation of these five trials was $\sim 1°$, roughly half of the observed standard deviation in our analysis. Therefore, recovered inflow longitudes are quite sensitive to fluctuations in the data. These fluctuations arise not only due to Poisson fluctuations but also from the Warm Breeze and other backgrounds, resulting in a somewhat larger observed standard deviation than that found from simulations that include only Poisson fluctuations. This explains why the derived inflow longitude from any one season shows fluctuations with respect to the the actual inflow longitude.

Another analysis that reveals the large effect of fluctuations is presented by Swaczyna et al. (2015). They also performed a χ^2 analysis, but used an alternative method of fitting the rate distribution as a function spin-phase latitude, as opposed to the latitudinal peak of the spin-phase distribution as done here. One of the interesting outcomes of the analysis is that the interstellar parameters derived from the χ^2 minimization of 2009 data were similar to results from previous work (e.g., Bzowski et al. 2012). Specifically, the derived inflow longitude was $77.7° \pm 1.0°$ and speed 24.5 ± 0.8 km s^{-1}, which is similar, within uncertainties, to the values shown

Table 1: Results of the $\tilde{\chi}^2$ minimization applied to the group 2 ($\epsilon \sim 0°$) data set in 2012-2014 used by Leonard et al. (2015).

	$\lambda_{ISN\infty}$ (°)	$V_{ISN\infty}$ (km/s)	$\beta_{ISN\infty}$ (°)	T_{ISN} (kK)
Optimum Value	75.8	25.4	-5.11	7.9
Fit Uncertainty	1.6	1.2	0.07	1.0
Stat. Uncertainty	0.04	0.03	0.002	0.5
Pointing Uncertainty	0.95	0.7	0.27	0.8
Total Uncertainty[a]	1.8	1.4	0.28	1.4

[a]The total uncertainties in the final row listed lie along the parameter tube and are therefore dependent on one another.

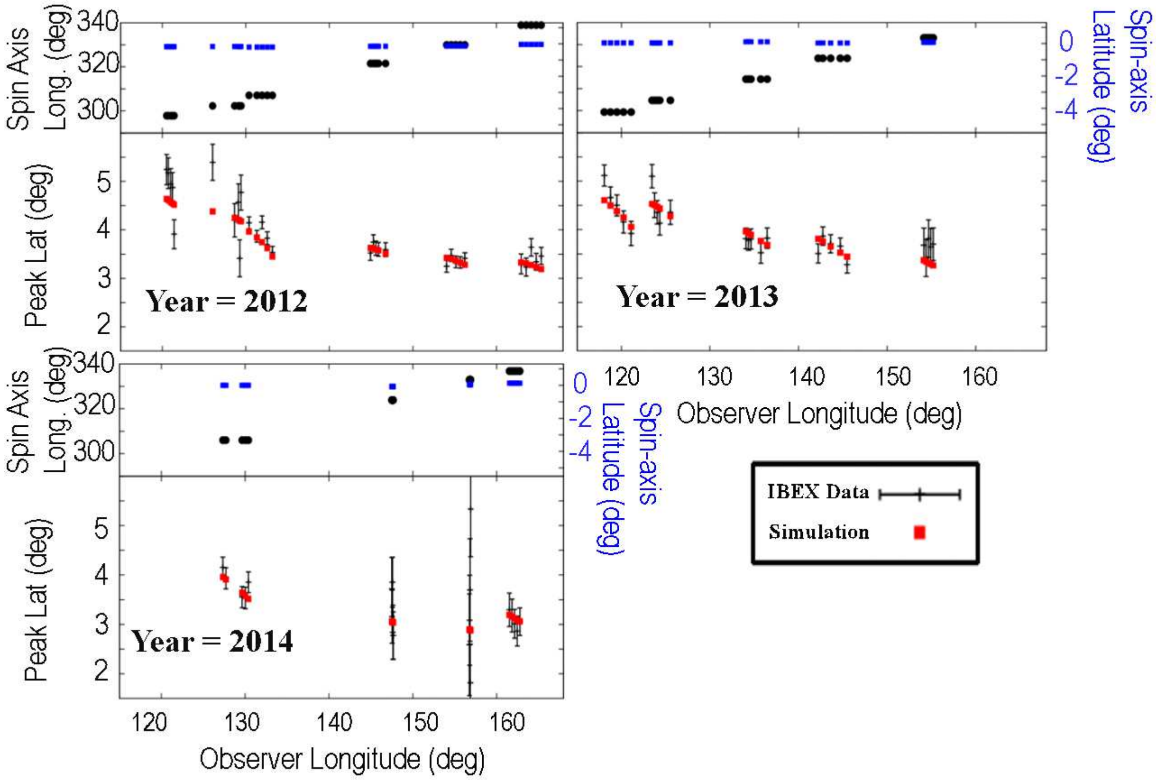

Fig. 4.— Peak latitudes, uncertainties (black error bars) and simulation results (red squares) for the optimum simulation that minimizes the $\tilde{\chi}^2$ in the analysis of data with $\epsilon_z \sim 0°$ in the years 2012-2014, as originally studied by Leonard et al. (2015). The uncertainties shown for the observations are taken from root-sum-square of Poisson counting statistical uncertainties and the pointing uncertainty of 0.05°. In each panel, the upper box shows the spin-axis longitude (black circles) and spin-axis latitude (blue squares) ϵ_z corresponding to the right-hand upper vertical-axis.

Table 2: Results of the $\tilde{\chi}^2$ minimization applied to the data from 2009-2013 with no restriction on the spin-axis (all values of ϵ included).

	$\lambda_{ISN\infty}$ (°)	$V_{ISN\infty}$ (km/s)	$\beta_{ISN\infty}$ (°)	T_{ISN} (kK)
Optimum Value	75.6	25.4	-5.12	8.0
Fit Uncertainty	1.0	0.8	0.04	0.9
Stat. Uncertainty	0.02	0.01	0.0007	0.5
Pointing Uncertainty	0.95	0.7	0.27	0.8
Total Uncertainty[a]	1.4	1.1	0.27	1.3

[a]The total uncertainties in the final row listed lie along the parameter tube and are therefore dependent on one another.

Table 3: Results of the $\tilde{\chi}^2$ minimization applied to each separate year analyzed.[a]

Year	$\lambda_{ISN\infty}$ (°)	$V_{ISN\infty}$ (km/s)	$\beta_{ISN\infty}$ (°)	T_{ISN} (kK)	$\tilde{\chi}^2$
2009	76.6 ± 2.7	24.8 ± 2.1	-5.1 ± 0.3	7.4 ± 2.0	1.89
2010	73.5 ± 2.5	27.0 ± 2.1	-5.2 ± 0.3	9.5 ± 2.4	1.15
2011	77.9 ± 3.5	23.8 ± 2.5	-5.0 ± 0.2	6.7 ± 2.2	1.40
2012	74.4 ± 2.1	26.4 ± 1.7	-5.2 ± 0.3	8.8 ± 1.9	1.82
2013	77.6 ± 2.4	24.1 ± 1.8	-5.0 ± 0.3	6.9 ± 1.7	1.32

[a]As in Table 1, the total uncertainties lie along the parameter tube and are therefore dependent on one another.

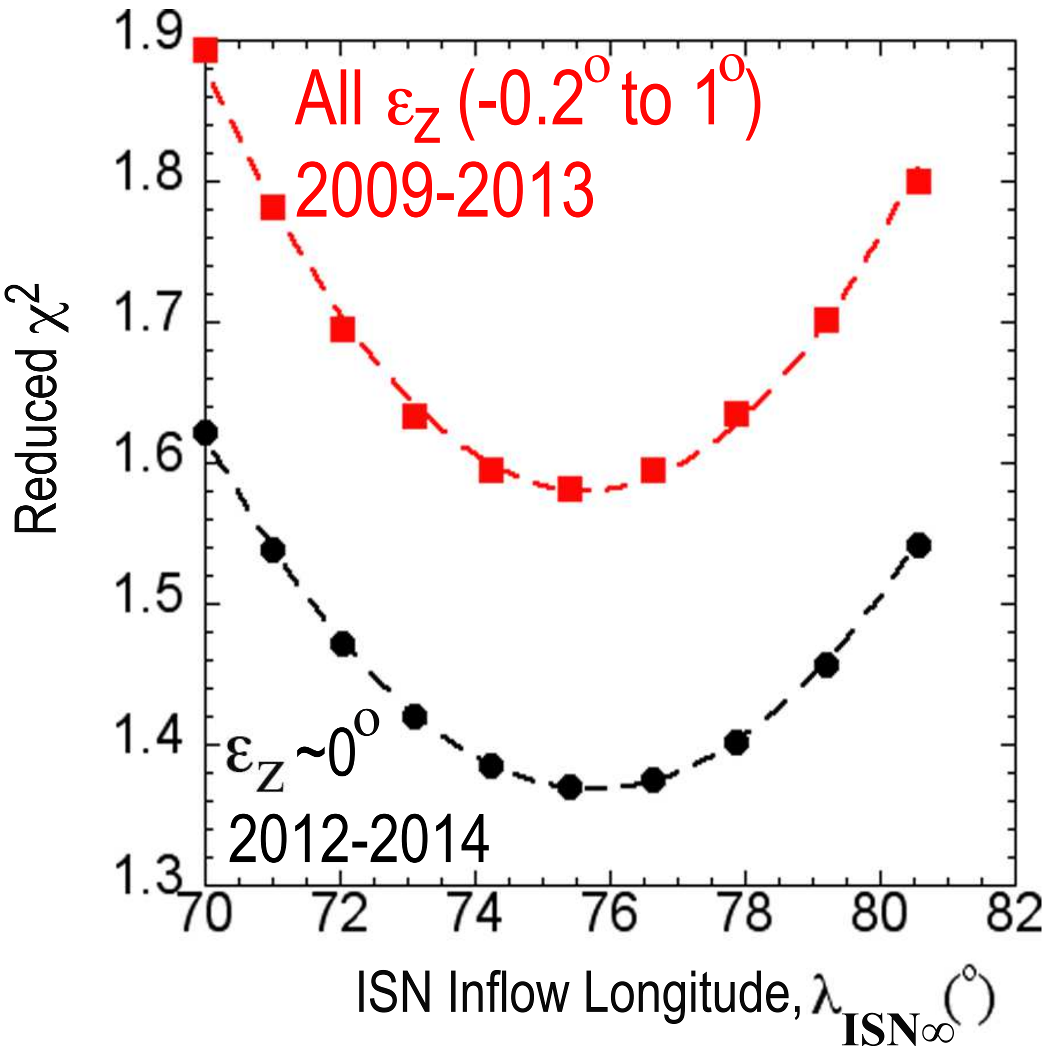

Fig. 5.— Reduced $\tilde{\chi}^2$ dependence (Red data points and red quadratic fit curve) of simulated versus observed peak distributions for the data set spanning all values of ϵ_z from $-0.2°$ to $1°$ over 2009-2013. Black data points and the quadratic fit line correspond to the fit to the data set studied by Leonard et al. (2015) from Figure 3. The $\tilde{\chi}^2$ minimum for the red points is found for an inflow longitude of $\lambda_{ISN\infty} = 75.6° \pm 1.4°$ which is comparable but with reduced uncertainty compared to the result derived in the fit to data from Leonard et al. (2015), $\lambda_{ISN\infty} = 75.8° \pm 1.8°$. The quadratic fit for the red curve (all values of ϵ_z) is given by $\tilde{\chi}^2(\lambda_{ISN\infty}) = A_0 + A_2(\lambda_{ISN\infty} - \lambda_0)^2$ where $A_0 = 1.58$, $A_2 = 0.0095$ and $\lambda_0 = 75.6°$.

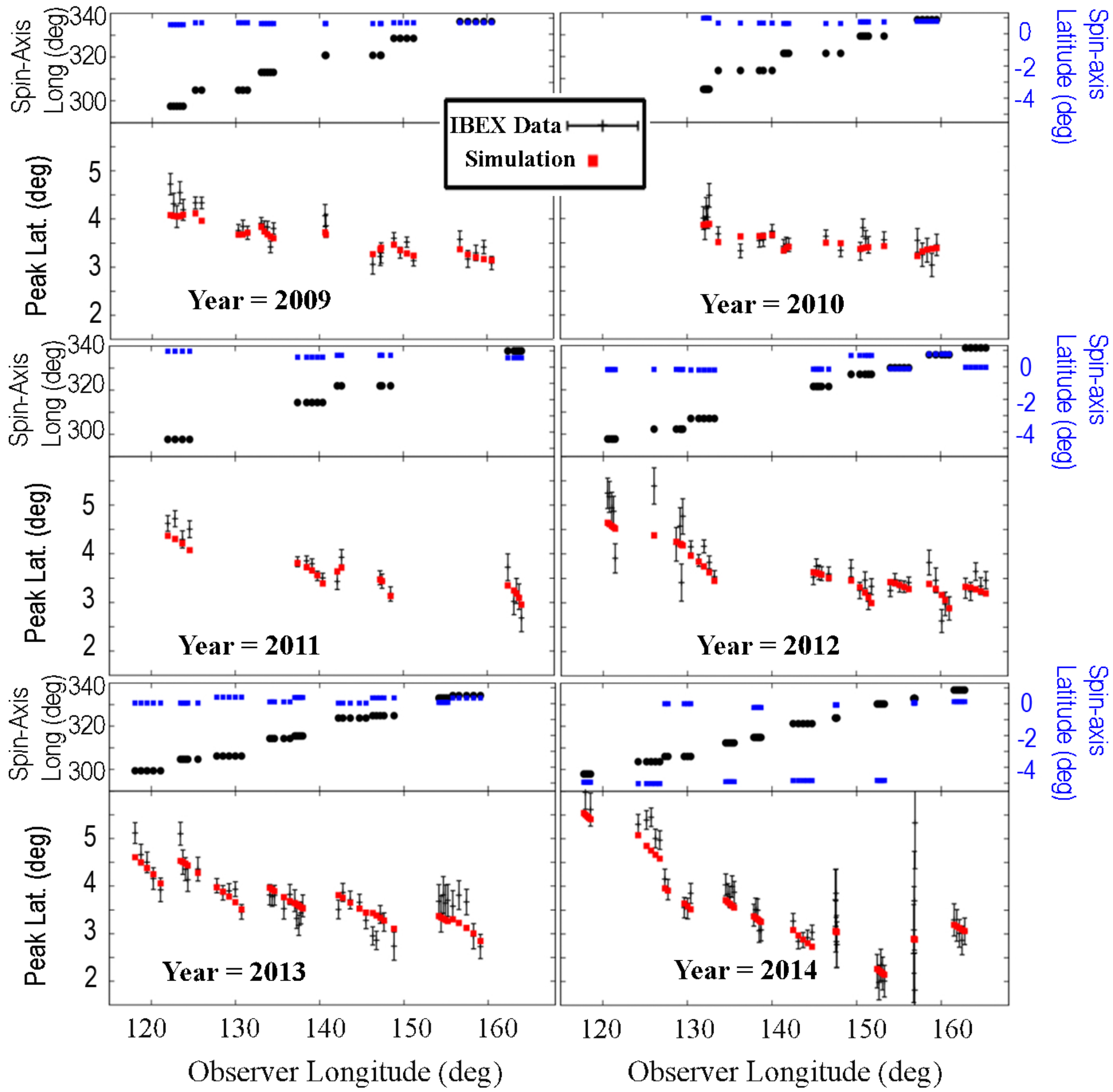

Fig. 6.— Peak latitudes, uncertainties (black error bars), and simulation results (red squares) for the optimum simulation that minimizes the $\tilde{\chi}^2$ in the analysis of all data (excluding outliers) from 2009-2013. We also show a comparison to the 2014 data, which was excluded due to the absence of a $\tilde{\chi}^2$ minimum in the parameter range studied. In each panel, the upper box shows the spin-axis longitude (black circles) and spin-axis latitude (blue squares) ϵ_z corresponding to the right-hand upper vertical-axis.

in Table 3 for 2009 (i.e., inflow longitude $76.6° \pm 2.7°$ and speed 24.8 ± 2.1 km s^{-1}). The fact that these results deviate from the average of 5-seasons is simply the effect of fluctuations in the data that include Poisson fluctuations, existence of the Warm Breeze and other fluctuations from additional backgrounds. Since our solutions along the parameter tube are highly degenerate, we require a large observational baseline to recover solutions with suitably low uncertainties to ascertain accurate interstellar parameters. Future work will allow further reductions in uncertainty.

Individual outliers are removed by identifying the individual data points for which the deviation between simulations and observations exceeds a threshold of 3.5 times the total uncertainty. Note that a single data point consists only of one of the five data points taken in a given orbit. There are 158 total data points, excluding outliers, taken over the 5 years. Because multiple simulations are used, outliers must have deviations that exceed the threshold for at least 30% of the longitude range over which simulations were run. While only two data points were found that systematically show such large deviations, the removal of these data points is essential, for they very strongly influence the χ^2 and therefore drive the fit parameters to a particular solution.

We have excluded the 2014 data from the analysis since during this year no $\tilde{\chi}^2$ minimum exists in the range of studied longitudes ($\lambda_{ISN\infty}$) from $71° - 81°$, and the $\tilde{\chi}^2$ is smallest for $\lambda_{ISN\infty} = 81°$. In 2014, the majority of data have spin axis tilts $\epsilon_z \sim -4.9°$, which appears to bias results significantly, possibly due to the influence of the Warm Breeze. In fact, when running the analysis for 2014 and including only data with spin axis tilts near the ecliptic ($\epsilon_z \sim 0°$), we find a $\tilde{\chi}^2$ minimum roughly consistent with the results in Table 1. This reinforces the hypothesis that the Warm Breeze may strongly influence data in 2014 when spin-axis tilts are well below the ecliptic. The data in 2014 remains under active investigation and is studied by Bzowski et al. (2015), but is not included in this $\tilde{\chi}^2$ minimization.

One of the interesting features seen in Figure 5 is that the reduced $\tilde{\chi}^2$ values are larger when we consider all data (red points and curve), as opposed to restricting the analysis to periods when $\epsilon_z \sim 0°$, as was done by Leonard et al. (2015). This shows that the agreement between simulations and observations is better when the data are restricted to $\epsilon_z \sim 0°$. Possible explanations for the larger deviation when no restriction is placed on the spin-axis latitude are that the Warm Breeze exerts a larger influence or that another background is present when the spin axis points well out of the ecliptic plane.

As in Figure 4, the simulation results in Figure 6 are sensitive to detailed characteristics of the spacecraft and sensor orientations. Finding time periods of low backgrounds and good observing introduces an unequal spacing of data points in observer longitude. There is a sawtooth pattern apparent in the simulations, particularly in 2012, 2013 and 2014. This sawtooth pattern arises because the spin-axis longitude and latitude have different discrete values in each orbit arc (the spacecraft undergoes a repointing maneuver in each orbit arc), while the observer longitude changes steadily through each orbit arc. As a consequence, the spin axis orientation and thus the IBEX viewing of the ISN flow change steadily over the course of each orbit arc.

5. Data Release.

IBEX data releases provide a critical vehicle for communicating in depth the results from IBEX, and supplying the Heliophysics, Astrophysics, and Space Science community with a record of analysis that is traceable and tractable. In Data release 9, we include the necessary information to determine ISN parameters. In particular, the release includes the IBEX ephemeris data, the spin-axis pointing data, and the observed and modeled peak locations for each of the runs included in the χ^2 analysis. We include results of analysis for both the 2012-2014 period with $\epsilon_z \sim 0°$ studied originally by Leonard et al. (2015) and the 2009-2013 period with a wide range of $\epsilon_z \sim -0.2° - 1°$. Additional IBEX data products and results spanning the coordinated set of papers in the Special Issue on interstellar neutrals (McComas et al. 2015) are included in the release, as also documented by Swaczyna et al. (2015) and Bzowski et al. (2015).

6. Conclusions

We have developed a model for numerically integrating analytic neutral atom trajectories through the detailed instrument response of IBEX-Lo. The model solves for the peak rate as a function of latitude during a spin-phase rotation of the IBEX spacecraft. Simulated peak latitudes are compared directly to observed peaks in the frame of the spacecraft. Therefore, ISN He parameters are derived rigorously through minimization of the χ^2 deviation between the simulated and observed quantities. The $\tilde{\chi}^2$ minimization is performed by varying the inflow longitude along the parameter tube (McComas et al. 2012b) and varying the inflow latitude across the parameter tube, with temperature and speed obtained from the characteristics along or perpendicular to the parameter tube.

This paper explores two complementary analyses using IBEX data and the numerically integrated IBEX-Lo response model. Our first analysis includes the periods studied by Leonard et al. (2015) in which the IBEX spin axis was within 0.2° of the ecliptic. Our second analysis includes all data from 2009 through 2013 excluding outliers (outside 3.5 standard deviation). Results from both $\tilde{\chi}^2$ minima are listed in the last two rows of Table 4 along with results from previous ISN He studies including Ulysses data analyzed at first by Witte et al. (2004) and re-analyzed by Bzowski et al. (2014) and Wood et al. (2015). Additionally, we compare these results along the parameter tube in Figure 7.

The data taken during 2014 with sizable spin-axis pointing out of the ecliptic ($\epsilon_z \sim -4.9°$) present a challenge in our analysis. Specifically, the fit using this 2014 data yields no overall minimum in the $\tilde{\chi}^2$ function in the range from $71° - 81°$ for simulated inflow longitudes. One hypothesis is that the data taken for $\epsilon_z \sim -4.9°$ is more strongly influenced by the Warm Breeze. This data set is under active study and is investigated by Bzowski et al. (2015).

It is notable that the results of our study are in close agreement with those of Bzowski et al. (2015), which analyzed all six years of IBEX data. The major differences between our study and the Bzowski et al. (2015) study are as follows: 1) Bzowski et al. (2015) adopted a test particle approach that takes into account the variation of ionization rates as a function of time along the ENA trajectories and follow trajectories from 150 AU; 2) Bzowski et al. (2015) subtract the Warm Breeze prior to fitting the primary component; and 3) Bzowski et al. (2015) do not fit the peaks of the distribution, but rather fit the detailed spin-phase distribution. Our technique, while complementary, is quite different from that applied by Bzowski et al. (2015). Möbius et al. (2015b) reveal a number of the differences in the approaches used. It is remarkable that the two methods result in such similar final results that are well within their respective uncertainties.

The larger baseline and reduced backgrounds compared to the Möbius et al. (2012), McComas et al. (2012b) and Bzowski et al. (2012) studies are critical in establishing the LISM parameters with smaller uncertainties. Future studies will allow further characterization of the primary and secondary interstellar distributions that inform not only the bulk parameters of the interstellar flow, but also the interstellar medium's interaction in the heliosheath and the nature of interstellar turbulence that might distort the observed helium velocity distributions.

The higher temperature and the derived speed of the LISM have a number of important implications that were detailed by McComas et al. (2015). We summarize and expand upon these points here:

- The LISM speed (25.4 ± 1.1 km/s) is between that of the LIC (~ 24 km/s) and G-Cloud (~ 30 km/s) from Redfield & Linsky (2008), suggesting the possibility that our heliosphere is currently in some sort of boundary region between the LIC and G-Cloud.

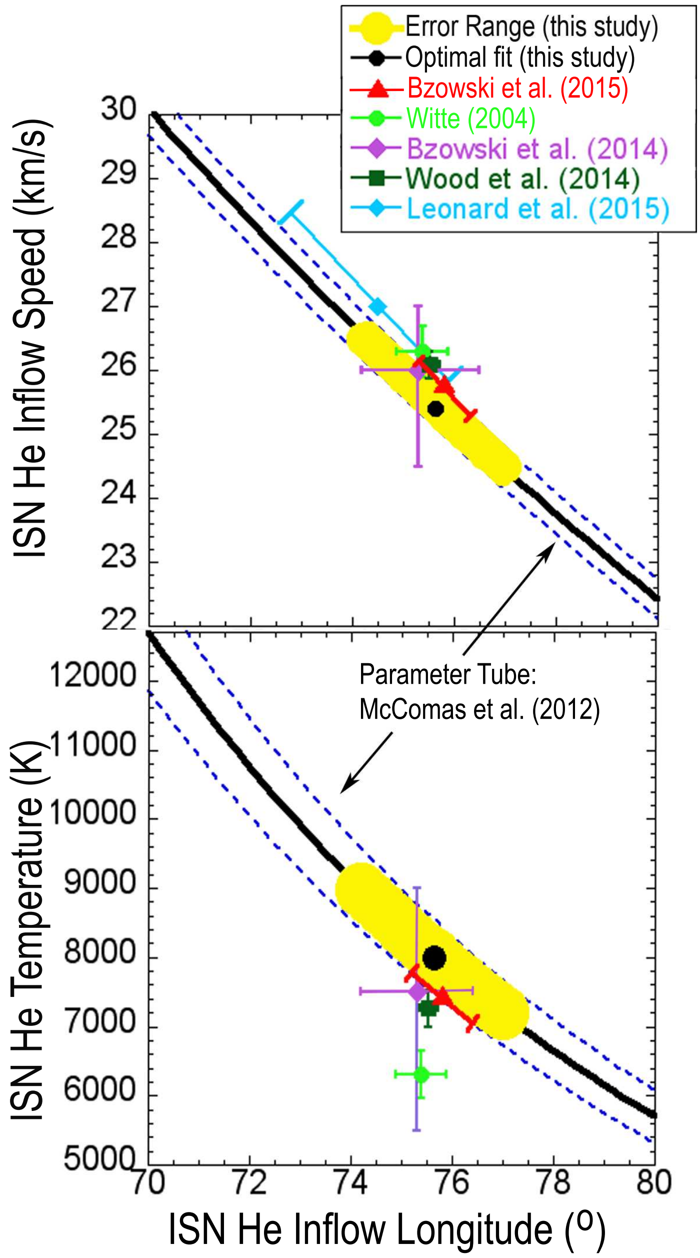

Fig. 7.— Results of analysis of ISN He inflow speed vs. inflow longitude (upper panel) and LISM inflow temperature vs. inflow longitude (lower panel) as listed in Table 4. The black point ("this study") refers to the analysis utilizing data from 2009 through 2013. The yellow regions along the parameter tubes indicate the uncertainty range found in performing the $\tilde{\chi}^2$ minimization. The parameter tube (from McComas et al. 2012b) is shown (black curve) along with the parameter tube uncertainty range (dashed blue curves).

- McComas et al. (2015) discuss the implications of the LISM speed and temperature for the bow shock. For example, Zieger et al. (2013) argue that there may be a region where a slow magnetosonic bow shock is possible. Within the context of a more traditional fast shock, the existence of 3 μG field strength, which was derived from the observed line-of-sight integrated plasma pressure (Schwadron et al. 2011, 2014) in the LISM, and 0.08 cm^{-3} LISM proton density suggests an Alfvén speed, v_A ~23 km/s. Therefore, if the LISM flow speed is 25 km/s, it is weakly super-Alfvénic, suggesting that a magnetosonic bow shock might exist, at least over a small region in front of the heliosphere. However, the existence of a stronger magnetic field ($\sim$ 4.6 μG, Burlaga & Ness 2013) in the LISM, would yield an even larger Alfven speed, $v_A \sim$ 35 km/s, which could preclude a fast magnetosonic shock ahead of the heliosphere. Additionally, Scherer & Fichtner (2014) include LISM He$^+$, which reduces the Alfven and fast magnetosonic speeds, and Zank et al. (2013) demonstrate the importance of ENAs in mediating the bow shock or bow wave.

- The warmer LISM is also consistent with remote sensing astronomical observations (Frisch et al. 2015), albeit within large uncertainties and variations depending on sightlines. LIC temperature ranges from 5700-8200 K toward ϵ CMa (Gry & Jenkins 2001), 8000 (+500-1000) K toward Sirius (Hébrard et al. 1999), and 7500 ± 1300 for the ensemble of LIC ultraviolet data (Redfield & Linsky 2008). Photoionization models predict a temperature gradient in the LIC and BC gas on the order of 5% (Slavin & Frisch 2002), so that the IBEX-Lo *in situ* measurement of the LIC temperature becomes an important comparison value for theoretical modeling of the morphology, equilibrium, and thermal stability of the LIC.

- The higher LISM temperature found here (8000 ± 1300 K) provides a valuable constraint on the heating and cooling mechanisms of the LIC, and the role of emissions from hot cloud interfaces in maintaining the helium and neon ionizations (Slavin & Frisch 2008).

- The direction of the LISM velocity vector determines the $\mathbf{B}_{ISM}$-$\mathbf{V}_{ISM}$ plane (Figure 8) that contains both the primary He inflow direction and the H inflow direction. Here, the interstellar magnetic field vector is $\mathbf{B}_{ISM}$ and the interstellar velocity vector is $\mathbf{V}_{ISM}$ so that the $\mathbf{B}_{ISM}$-$\mathbf{V}_{ISM}$ plane constains these vectors. The H inflow direction is more strongly affected by secondary interactions in the heliosheath than the He inflow. Therefore, the $\mathbf{B}_{ISM}$-$\mathbf{V}_{ISM}$ plane should contain the deflection vector of H relative to He (Lallement et al. 2005). As shown in Figure 8, the inflow He vector results in a $\mathbf{B}_{ISM}$-$\mathbf{V}_{ISM}$ plane that, within uncertainty, contains the center of the IBEX ribbon for energy steps up to 2.7 keV. The notable departure at 4.3 keV is not surprising given that the ribbon exhibits enormous variability at this energy step and ceases to be well represented by a circular structure. The result shown in Figure 8 reveals consistency between the inflow direction of He and the direction of the LISM magnetic field as the center of the IBEX ribbon.

We introduced the paper by noting that previous work on IBEX neutral atom analysis has relied, in part, on an approach utilizing closed form analytic approximations (Lee et al. 2012, 2015) for the distribution of neutral atoms observed in the Earth's reference frame. This approach has numerous advantages, particularly in offering insights that have guided analysis of interstellar flow properties. However, the approach also has some limitations. The use of small-angle expansions to achieve closed form solutions and the adoption of an Earth reference frame complicates analysis. The approach we have taken offers an extension of the original analytic approach formulated by Lee et al. (2012) and applied by Möbius et al. (2012). We directly integrate over the IBEX-Lo response in the spacecraft reference frame, providing the basis for a more straightforward and more accurate comparison between model results and IBEX data. Equipped with this tool, we have re-analyzed IBEX data over 5 years. Results agree with and reinforce the results of recent IBEX analyses (e.g., Leonard et al. 2015; McComas et al. 2015; Bzowski et al. 2015; Möbius et al. 2015a) and Ulysses re-analyses (Wood et al. 2015; Bzowski et al. 2014). Specifically, we find agreement with the Ulysses He inflow direction and speed and a hotter temperature than originally inferred by Witte et al. (2004).

We are grateful to the many individuals who have made the IBEX project possible. This work is supported by the Interstellar Boundary Explorer mission as a part of NASAs Explorer Program and partially by NASA SR&T Grant NNG06GD55G, the Swiss National Science Foundation, PRODEX, and the Polish National Science Center grant 2012-06-M-ST9-00455.

REFERENCES

Bochsler, P., Petersen, L., Möbius, E., Schwadron, N. A., Wurz, P., Scheer, J. A., Fuselier, S. A., McComas, D. J., Bzowski, M., & Frisch, P. C. 2012, Astrophys. J. Suppl., 198, 13

Burlaga, L. F. & Ness, N. F. 2013, Astrophys. J., 765, 35

Bzowski, M., Kubiak, M. A., Hłond, M., Sokół, J. M., Banaszkiewicz, M., & Witte, M. 2014, Astron. Astrophys., 569, A8

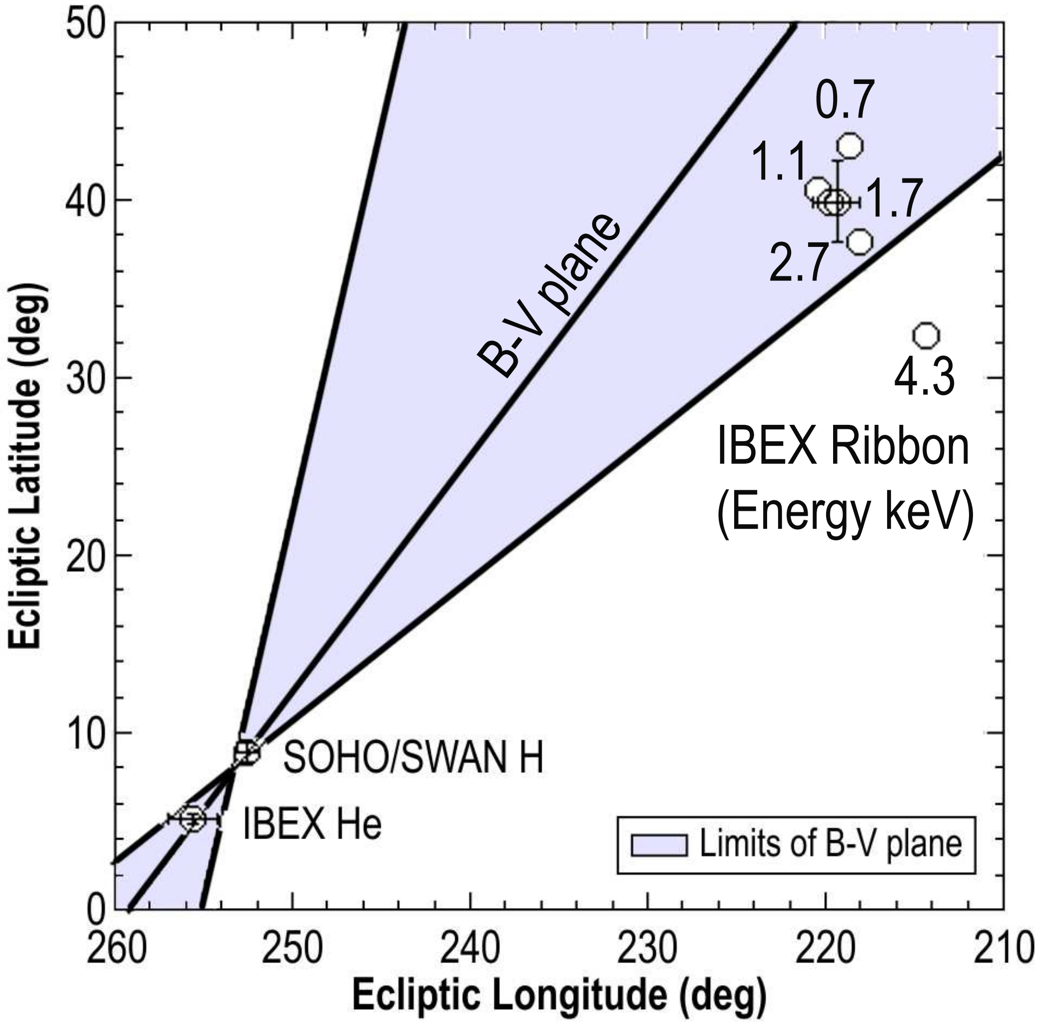

Fig. 8.— The H flow direction from SOHO/SWAN (Lallement et al. 2005, 2010) is plotted along with the He flow direction derived here. The plane containing both the H inflow direction and the primary He inflow direction is called the $\mathbf{B}_{ISM}$-$\mathbf{V}_{ISM}$ plane since it is thought to contain both the interstellar magnetic field vector $\mathbf{B}_{ISM}$ and the interstellar velocity vector $\mathbf{V}_{ISM}$. The H inflow direction is more strongly affected by secondary interactions in the heliosheath than the He inflow. Therefore, the $\mathbf{B}_{ISM}$-$\mathbf{V}_{ISM}$ plane should contain the deflection vector of H relative to He (Lallement et al. 2005). The shaded region shows the limits of the $\mathbf{B}_{ISM}$-$\mathbf{V}_{ISM}$ plane, which appears roughly consistent with the orientation of the IBEX ribbon (Funsten et al. 2013). The center (open circles without error bars) of the IBEX ribbon is shown as derived from a circular fit at each energy step of IBEX-Hi. We also show the mean center and uncertainty of the IBEX ribbon (the ribbon point with an error bar) reported by Funsten et al. (2013).

Bzowski, M., Kubiak, M. A., Möbius, E., Bochsler, P., Leonard, T., Heirtzler, D., Kucharek, H., Sokół, J. M., Hłond, M., Crew, G. B., Schwadron, N. A., Fuselier, S. A., & McComas, D. J. 2012, Astrophys. J. Suppl., 198, 12

Bzowski, M., Sokół, J. M., Kubiak, M. A., & Kucharek, H. 2013a, Astron. Astrophys., 557, A50

Bzowski, M., Sokół, J. M., Tokumaru, M., Fujiki, K., Quémerais, E., Lallement, R., Ferron, S., Bochsler, P., & McComas, D. J. 2013b, Solar Parameters for Modeling the Interplanetary Background (Springer), 67

Bzowski, M., Swaczyna, P., Kubiak, M. A., Sokół, J. M., Moebius, E., Leonard, T., Heirtzler, D., Schwadron, N. A., Fuselier, S., Kucharek, H., Galli, A., Wurz, P., & McComas, D. J. 2015, Astrophys. J. Suppl., this volume

Fahr, H. J. 1979, Astron. Astrophys., 77, 101

Frisch, P. C., Bzowski, M., Drews, C., Leonard, T., Livadiotis, G., McComas, D. J., Möbius, E., Schwadron, N., & Sokół, J. M. 2015, Astrophys. J., 801, 61

Frisch, P. C., Bzowski, M., Livadiotis, G., McComas, D. J., Moebius, E., Mueller, H.-R., Pryor, W. R., Schwadron, N. A., Sokół, J. M., Vallerga, J. V., & Ajello, J. M. 2013, Science, 341, 1080

Funsten, H. O., Allegrini, F., Bochsler, P., Dunn, G., Ellis, S., Everett, D., Fagan, M. J., Fuselier, S. A., Granoff, M., Gruntman, M., Guthrie, A. A., Hanley, J., Harper, R. W., Heirtzler, D., Janzen, P., Kihara, K. H., King, B., Kucharek, H., Manzo, M. P., Maple, M., Mashburn, K., McComas, D. J., Moebius, E., Nolin, J., Piazza, D., Pope, S., Reisenfeld, D. B., Rodriguez, B., Roelof, E. C., Saul, L., Turco, S., Valek, P., Weidner, S., Wurz, P., & Zaffke, S. 2009, Space Sci. Rev., 146, 75

Funsten, H. O., DeMajistre, R., Frisch, P. C., Heerikhuisen, J., Higdon, D. M., Janzen, P., Larsen, B. A., Livadiotis, G., McComas, D. J., Möbius, E., Reese, C. S., Reisenfeld, D. B., Schwadron, N. A., & Zirnstein, E. J. 2013, Astrophys. J., 776, 30

Fuselier, S. A., Allegrini, F., Bzowski, M., Dayeh, M. A., Desai, M., Funsten, H. O., Galli, A., Heirtzler, D., Janzen, P., Kubiak, M. A., Kucharek, H., Lewis, W., Livadiotis, G., McComas, D. J., Möbius, E., Petrinec, S. M., Quinn, M., Schwadron, N., Sokół, J. M., Trattner, K. J., Wood, B. E., & Wurz, P. 2014, Astrophys. J., 784, 89

Fuselier, S. A., Bochsler, P., Chornay, D., Clark, G., Crew, G. B., Dunn, G., Ellis, S., Friedmann, T., Funsten, H. O., Ghielmetti, A. G., Googins, J., Granoff, M. S., Hamilton, J. W., Hanley, J., Heirtzler, D., Hertzberg, E., Isaac, D., King, B., Knauss, U., Kucharek, H., Kudirka, F., Livi, S., Lobell, J., Longworth, S., Mashburn, K., McComas, D. J., Möbius, E., Moore, A. S., Moore, T. E., Nemanich, R. J., Nolin, J., O'Neal, M., Piazza, D., Peterson, L., Pope, S. E., Rosmarynowski, P., Saul, L. A., Scherrer, J. R., Scheer, J. A., Schlemm, C., Schwadron, N. A., Tillier, C., Turco, S., Tyler, J., Vosbury, M., Wieser, M., Wurz, P., & Zaffke, S. 2009, Space Sci. Rev., 146, 117

Galli, A., Wurz, P., Fuselier, S. A., McComas, D. J., Bzowski, M., Sokół, J. M., Kubiak, M. A., & Möbius, E. 2014, Astrophys. J., 796, 9

Galli, A., Wurz, P., Park, J., Kucharek, H., Möbius, E., Schwadron, N. A., Sokół, J. M., Bzowski, M., Kubiak, M. A., Swaczyna, P., Fuselier, S., & McComas, D. J. 2015, Astrophys. J. Suppl., Under review

Gry, C. & Jenkins, E. B. 2001, Astron. Astrophys., 367, 617

Hébrard, G., Mallouris, C., Ferlet, R., Koester, D., Lemoine, M., Vidal-Madjar, A., & York, D. 1999, Astron. Astrophys., 350, 643

Katushkina, O. A., Izmodenov, V. V., Alexashov, D. B., Schwadron, N. A., & McComas, D. J. 2015, Astrophys. J. Suppl., In Press, This Volume

Katushkina, O. A., Izmodenov, V. V., Wood, B. E., & McMullin, D. R. 2014, Astrophys. J., 789, 80

Kubiak, M. A., Bzowski, M., Sokół, J. M., Swaczyna, P., Grzedzielski, S., Alexashov, D. B., Izmodenov, V. V., Möbius, E., Leonard, T., Fuselier, S. A., Wurz, P., & McComas, D. J. 2014, Astrophys. J. Suppl., 213, 29

Lallement, R. & Bertaux, J. L. 2014, Astron. Astrophys., 565, A41

Lallement, R., Quémerais, E., Bertaux, J. L., Ferron, S., Koutroumpa, D., & Pellinen, R. 2005, Science, 307, 1447

Lallement, R., Quémerais, E., Koutroumpa, D., Bertaux, J.-L., Ferron, S., Schmidt, W., & Lamy, P. 2010, Twelfth International Solar Wind Conference, 1216, 555

Lee, M. A., Kucharek, H., Möbius, E., Wu, X., Bzowski, M., & McComas, D. 2012, Astrophys. J. Suppl., 198, 10

Lee, M. A., öbius, E. M., et al. 2015, Astrophys. J. Suppl., this volume

Leonard, T. W., Möbius, E., Bzowski, M., Fuselier, S. A., Heirtzler, D., Kubiak, M. A., Kucharek, H., Lee, M. A., McComas, D. J., Schwadron, N. A., & Wurz, P. 2015, Astrophys. J., In Press

McComas, D. J., Alexashov, D., Bzowski, M., Fahr, H., Heerikhuisen, J., Izmodenov, V., Lee, M. A., Möbius, E., Pogorelov, N., Schwadron, N. A., & Zank, G. P. 2012a, Science, 336, 1291

McComas, D. J., Allegrini, F., Bochsler, P., Bzowski, M., Collier, M., Fahr, H., Fichtner, H., Frisch, P., Funsten, H. O., Fuselier, S. A., Gloeckler, G., Gruntman, M., Izmodenov, V., Knappenberger, P., Lee, M., Livi, S., Mitchell, D., Möbius, E., Moore, T., Pope, S., Reisenfeld, D., Roelof, E., Scherrer, J., Schwadron, N., Tyler, R., Wieser, M., Witte, M., Wurz, P., & Zank, G. 2009, Space Sci. Rev., 146, 11

McComas, D. J., Bzowski, M., Frisch, P., Fuselier, S. A., Kubiak, M. A., Kucharek, H., Leonard, T., Möbius, E., Schwadron, N. A., Sokół, J. M., Swaczyna, P., & Witte, M. 2015, Astrophys. J., 801, 28

McComas, D. J., Bzowski, M., Galli, A., Katushkina, O. A., Kucharek, H., Lee, M., Moebius, E., Park, J., Rodriguez, D., Schwadron, N., Sokół, J. M., Swaczyna, P., & Wood, B. 2015, Astrophys. J. Suppl., In Press

McComas, D. J., Dayeh, M. A., Allegrini, F., Bzowski, M., DeMajistre, R., Fujiki, K., Funsten, H. O., Fuselier, S. A., Gruntman, M., Janzen, P. H., Kubiak, M. A., Kucharek, H., Livadiotis, G., Möbius, E., Reisenfeld, D. B., Reno, M., Schwadron, N. A., Sokół, J. M., & Tokumaru, M. 2012b, Astrophys. J. Suppl., 203, 1

Möbius, E., Bochsler, P., Bzowski, M., Crew, G. B., Funsten, H. O., Fuselier, S. A., Ghielmetti, A., Heirtzler, D., Izmodenov, V. V., Kubiak, M., Kucharek, H., Lee, M. A., Leonard, T., McComas, D. J., Petersen, L., Saul, L., Scheer, J. A., Schwadron, N., Witte, M., & Wurz, P. 2009, Science, 326, 969

Möbius, E., Bochsler, P., Bzowski, M., Heirtzler, D., Kubiak, M. A., Kucharek, H., Lee, M. A., Leonard, T., Schwadron, N. A., Wu, X., Fuselier, S. A., Crew, G., McComas, D. J., Petersen, L., Saul, L., Valovcin, D., Vanderspek, R., & Wurz, P. 2012, Astrophys. J. Suppl., 198, 11

Möbius, E., Bzowski, M., Chalov, S., Fahr, H.-J., Gloeckler, G., Izmodenov, V., Kallenbach, R., Lallement, R., McMullin, D., Noda, H., Oka, M., Pauluhn, A., Raymond, J., Ruciński, D., Skoug, R., Terasawa, T., Thompson, W., Vallerga, J., von Steiger, R., & Witte, M. 2004, Astron. Astrophys., 426, 897

Möbius, E., Bzowski, M., Frisch, P. C., Fuselier, S. A., Heirtzler, D., Kubiak, M. A., Kucharek, H., Lee, M. A., Leonard, T., McComas, D. J., Schwadron, N. A., Sokół, J. M., & Wurz, P. 2015a, Astrophys. J. Suppl., In press

Möbius, E., Bzowski, M., Fuselier, S. A., et al. 2015b, in Proc. of the 13th AIAC, J. of Phys. Conf. Series, ed. G. Zank et al., 012019

Park, J., Kucharek, H., Möbius, E., Leonard, T., Bzowski, M., Sokół, J. M., Kubiak, M. A., Fuselier, S. A., & McComas, D. J. 2014, Astrophys. J., 795, 97

Park, J., Kucharek, H., Möbius, E., et al. 2015, Astrophys. J. Suppl., this volume

Redfield, S. & Linsky, J. L. 2008, Astrophys. J., 673, 283

Rodríguez Moreno, D., Wurz, P., Saul, L., Bzowski, M., Kubiak, M., Sokół, J., Frisch, P., Fuselier, S., McComas, D., Möbius, E., & Schwadron, N. 2014, Entropy, 16, 1134

Rodríguez Moreno, D. F., Wurz, P., Saul, L., Bzowski, M., Kubiak, M. A., Sokół, J. M., Frisch, P., Fuselier, S. A., McComas, D. J., Möbius, E., & Schwadron, N. 2013, Astron. Astrophys., 557, A125

Scherer, K. & Fichtner, H. 2014, Astrophys. J., 782, 25

Schwadron, N. A., Allegrini, F., Bzowski, M., Christian, E. R., Crew, G. B., Dayeh, M., DeMajistre, R., Frisch, P., Funsten, H. O., Fuselier, S. A., Goodrich, K., Gruntman, M., Janzen, P., Kucharek, H., Livadiotis, G., McComas, D. J., Moebius, E., Prested, C., Reisenfeld, D., Reno, M., Roelof, E., Siegel, J., & Vanderspek, R. 2011, Astrophys. J., 731, 56

Schwadron, N. A., Crew, G., Vanderspek, R., Allegrini, F., Bzowski, M., Demagistre, R., Dunn, G., Funsten, H., Fuselier, S. A., Goodrich, K., Gruntman, M., Hanley, J., Heerikhuisen, J., Heirtlzer, D., Janzen, P., Kucharek, H., Loeffler, C., Mashburn, K., Maynard, K., McComas, D. J., Moebius, E., Prested, C., Randol, B., Reisenfeld, D., Reno, M., Roelof, E., & Wu, P. 2009, Space Sci. Rev., 146, 207

Schwadron, N. A., Moebius, E., Fuselier, S. A., McComas, D. J., Funsten, H. O., Janzen, P., Reisenfeld, D., Kucharek, H., Lee, M. A., Fairchild, K., Allegrini, F., Dayeh, M., Livadiotis, G., Reno, M., Bzowski, M., Sokół, J. M., Kubiak, M. A., Christian, E. R., DeMajistre, R., Frisch, P., Galli, A., Wurz, P., & Gruntman, M. 2014, Astrophys. J. Suppl., 215, 13

Schwadron, N. A., Moebius, E., Kucharek, H., Lee, M. A., French, J., Saul, L., Wurz, P., Bzowski, M., Fuselier, S. A., Livadiotis, G., McComas, D. J., Frisch, P., Gruntman, M., & Mueller, H. R. 2013, Astrophys. J., 775, 86

Slavin, J. D. & Frisch, P. C. 2002, Astrophys. J., 565, 364

—. 2008, Astron. Astrophys., 491, 53

Sokół, J., Bzowski, M., Kubiak, M., Swaczyna, P., Galli, A., Wurz, P., Moebius, E., Kucharek, H., Fuselier, S., & McComas, D. 2015a, Astrophys. J. Suppl., In Work

Sokół, J., Kubiak, M. A., Bzowski, M., & Swaczyna, P. 2015b, Astrophys. J. Suppl., this volume

Swaczyna, P., Bzowski, M., Kubiak, M. A., Sokół, J. M., Möbius, E., Leonard, T., Heirtzler, D., Kucharek, H., Schwadron, N. A., Fuselier, S. A., & McComas, D. J. 2015, Astrophys. J. Suppl., this volume

Thomas, G. E. 1978, Annu. Rev. Earth Planet. Sci., 6, 173

Witte, M. 2004, Astron. Astrophys., 426, 835

Witte, M., Banaszkiewicz, M., Rosenbauer, H., & McMullin, D. 2004, Advances in Space Research, 34, 61

Wood, B. E., Müller, H.-R., & Witte, M. 2015, Astrophys. J., 801, 62

Wu, F. M. & Judge, D. L. 1979, Astrophys. J., 231, 594

Zank, G. P., Heerikhuisen, J., Wood, B. E., Pogorelov, N. V., Zirnstein, E., & McComas, D. J. 2013, Astrophys. J., 763, 20

Zieger, B., Opher, M., Schwadron, N. A., McComas, D. J., & Tóth, G. 2013, Geophys. Res. Lett., 40, 2923

Table 4. ISN flow parameters using direct ISN He flow observations by either the Ulysses or IBEX spacecraft. (J2000 coordinates used throughout) .

Publication	$\lambda_{ISN\infty}$ (°)	$V_{ISN\infty}$ (km/s)	$\beta_{ISN\infty}$ (°)	T_{ISN} (kK)	Spacecraft
Witte et al. (2004)	75.4 ± 0.5	26.3 ± 0.4	-5.2 ± 0.2	6.30 ± 0.34	Ulysses
Bzowski et al. (2014)	$75.3 + 1.2(-1.1)$	$26.0 + 1.0(-1.5)$	-6.0 ± 1.0	$7.5 + 1.5(-2.0)$	Ulysses
Wood et al. (2015)	75.54 ± 0.19	26.08 ± 0.21	-5.44 ± 0.24	7.26 ± 0.27	Ulysses
Leonard et al. (2015)[a]					
($\epsilon_z \sim 0$, 2012-14)	74.5 ± 1.7	$27.0 + 1.4(-1.3)$	-5.2 ± 0.3		IBEX
McComas et al. (2015)	~ 75	~ 26	~ -5	$7 - 9.5$	IBEX
Bzowski et al. (2015)[a]					
($\epsilon_z \sim 0$, 2012-14)	75.3 ± 0.6	26.7 ± 0.5	-5.14 ± 0.16	8.15 ± 0.39	IBEX
Bzowski et al. (2015)[a]					
(ϵ_z, no restriction, 2009-14)	75.8 ± 0.5	25.8 ± 0.4	-5.17 ± 0.10	7.44 ± 0.26	IBEX
this study[a]					
($\epsilon_z \sim 0$, 2012-14)	75.8 ± 1.8	25.4 ± 1.4	-5.11 ± 0.28	7.9 ± 1.4	IBEX
this study[a]					
(ϵ_z, no restriction, 2009-13)	75.6 ± 1.4	25.4 ± 1.1	-5.12 ± 0.27	8.0 ± 1.3	IBEX

[a]As in Table 1, the total uncertainties lie along the parameter tube and are therefore dependent on one another.